This is an accepted manuscript entitled “Stationary Bubble Formation and Marangoni Convection Induced by CW Laser Heating of a Single Gold Nanoparticle”, published in *Nanoscale*, 9 (**2017**), 719-730

To see the published version, click a link below:

https://doi.org/10.1039/C6NR07990C

Stationary Bubble Formation and Marangoni Convection Induced by CW Laser Heating of a Single Gold Nanoparticle

Kenji Setoura, Syoji Ito*, and Hiroshi Miyasaka*

Division of Frontier Materials Science and Center for Promotion of Advanced Interdisciplinary Research, Graduate School of Engineering Science, Osaka University, Toyonaka, Osaka 560-8531, Japan

*Corresponding authors: sito@chem.es.osaka-u.ac.jp, miyasaka@chem.es.osaka-u.ac.jp

*Electronic supplementary information (ESI) is available

Graphical abstract 4 × 8 cm

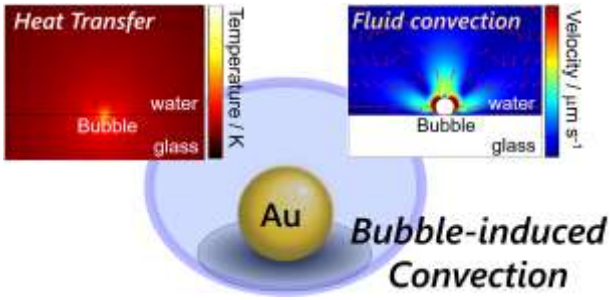

We have elucidated the spatial distribution of the temperature gradient and the corresponding convective velocity around a stationary bubble produced by CW laser heating of a single gold nanoparticle.

ABSTRACT

Gold nanoparticles (Au NPs) efficiently convert incident light into heat under the resonant condition of localized surface plasmon. Controlling mass transfer through plasmonic heating of Au NPs has potential applications such as manipulation and fabrication within a small space. Here, we describe the formation of stationary microbubbles and subsequent fluid convection induced by CW laser heating of Au NPs in water. Stationary bubbles about 1 – 20 μm in diameter were produced by irradiating individual Au NPs with a CW laser. Spatial profiles and velocity distribution of fluid convection around the microbubbles were visualized by wide-field fluorescence imaging of tracer nanospheres. To evaluate the bubble-induced convection, numerical simulations were performed on the basis of general heat diffusion and Navier-Stokes equations. A comparison between experimental and computational results revealed that a temperature derivative of surface tension at the bubble surface is a key factor to control the fluid convection. Temperature differences of a few Kelvin at the bubble surface resulted in convective velocities ranging from 10^2 to 10^3 μm s^{-1}. The convective velocity gradually saturated with increasing temperature differences up to several Kelvin. This article covers both natural and Marangoni convection induced by plasmonic heating of Au NPs.

KEYWORDS: Gold nanoparticles; Localized surface plasmon; Photothermal effect; Stationary bubble; Fluid convection.

INTRODUCTION

Noble metal nanoparticles (NPs) have been attracting much attention in the field of photoscience from various viewpoints. One of the characteristic features of noble metal NPs is the localization and enhancement of optical fields arising from Localized Surface Plasmon Resonance (LSPR)[1–3]. Photoexcitation of LSPR band promotes 10^6-fold enhancement of incident electric field in near-field regime. This field enhancement effect has been widely utilized as nanoscale optical antennas for photochemical reactions[4,5] and surface enhanced spectroscopy[6,7]. Another feature of noble metal NPs is their effective photothermal conversion efficiency. The photo-energy absorbed by NPs turns into heat via electron-phonon coupling within a few picosecond after the photoexcitation[8,9]. This rapid photothermal conversion is of great use as nanoscale heat sources. Among various noble metals, gold nanoparticles (Au NPs) are utilized as ideal local heaters because of their physicochemical stability and high conversion efficiency[10]. Elevation in local temperature through plasmonic heating of Au NPs leads to potential applications such as photothermal cancer therapy[11], photothermal imaging[12,13], and nanofabrication[14,15].

Because photoresponses including the surrounding medium of NPs is strongly dependent on the temperature of NPs, excitation light intensity is an important factor in the application of the photothermal effect. Temperature of Au NPs under laser illumination with 10^5- 10^7 W cm^{-2} is more than 10^3 K, leading to melting of NPs and/or evaporation of surrounding matrices. By irradiating Au NPs inside a tumor with pulsed lasers[16,17], Lukianova-Hleb *et al.* applied transient vapor bubbles generated via the evaporation of the medium surrounding NPs to the cancer therapy and drug delivery. Dynamics and mechanism of the bubble formation around heated NPs have been also investigated by means of the time-resolved X-ray scattering[18] and transient absorption spectroscopy[19,20]. These studies revealed that transient vapor bubbles in aqueous medium was

produced by the spinodal decomposition of surrounding water adjacent NPs surface at temperatures around 550 K[18,19,21,22] and the lifetime was in a few tens of nanoseconds, depending on the pulse width and excitation intensities.

Not only the pulsed excitation but also the CW laser irradiation can lead to the formation of bubbles[23,24] in the stationary state[25,26] around Au NPs in water. This stationary bubble can induce thermal convections of fluid around the focal spot of a laser beam (Scheme 1), which has emerged as a method to control the motion of fluid in microscopic region[27]. In general, thermal convection of fluid can be classified into two cases: natural convection and Marangoni convection. The former natural convection arises from buoyancy force generated by the density difference of liquid in the temperature gradient. Under the CW laser irradiation of a single Au NP in water, the convective velocity of the natural convection is ca. 10 nm s^{-1} around the single NP[28] and, at most, 1.0 μm s^{-1} in a dense array consisting of Au nanostructures[29]. Accordingly, the natural convection has small contribution for micro-manipulation or micro-fabrication. On the other hand, the latter Marangoni convection, originating from the surface tension of stationary bubbles, has much higher convective velocities[30,31] such as 1000 μm s^{-1}. By utilizing the Marangoni convection through plasmonic heating of Au NPs, several applications such as controlling fluid flow in microfluidic channels[30], assembling of colloidal nanoparticles[31–34], size selection of polystyrene beads[35], and crystallization of glycine[36] have been demonstrated.

For advanced applications of the local heating, basic physical features of the Marangoni convection are of crucially importance. Along this line in the present work, we have investigated the formation of stationary microbubbles and subsequent fluid convection induced by CW laser heating of individual Au NPs in water by employing experimental methods and numerical simulation. Fluid convection around the stationary bubble was experimentally visualized by wide-

field fluorescence imaging of polystyrene nanoparticles (FL-beads) as tracers, of which results were analyzed by numerical simulations of thermal convection on the basis of general heat diffusion and Navier-Stokes equation. By integrating the present results with our previous works on the thermometry of single NPs[37] and aggregates consisting of Au NPs[38], and bubble formation in water triggered by CW and pulsed laser irradiation[19,39], we have presented a model of photothermal convection by including all the components such as a single Au NP, the bubble, water, and a glass substrate.

MATERIALS and METHODS

Sample Preparation. The specimen was prepared in the following manner. Aqueous suspension of Au NPs with nominal diameters of 150 nm (EMGC 150, British Biocell International) were used as received. The particle images were acquired by a scanning electron microscope (SEM) and the corresponding size distributions are shown in Figure S1 in Electronic Supplementary Information (ESI). Glass coverslips (24 × 32 × 0.17 mm, Matsunami) were put into acetone in a small vessel and sonicated for 30 min, followed by immersion in 5 wt % aqueous solution of sodium hydrate for 30 min to purify the surface. After rinsing them with ultrapure water, the coverslips were dried with a nitrogen gun. Then Au NPs were spin-coated onto the well-cleaned coverslips. The Au NPs-coated coverslips were washed three times with ultrapure water on the spin coater. In addition to this sample preparation, Au NPs were submerged in medium, in a 120 μL chamber consisting of two coverslips and a 0.3 mm thick silicone rubber spacer. To observe the formation of stationary bubbles, ultrapure water was used as a surrounding medium. For visualization of fluid convection, a 0.05 wt % aqueous colloidal solution of dyes-loaded polystyrene nanospheres (F8795, 40-nm-diameter, Molecular Probes) was employed as tracer

nanospheres.

Optical Measurements. The specimen of coverslips was mounted on an *x*-*y* scanning stage (BIOS-150T, Sigma) of an inverted optical microscope (IX-70, Olympus). A schematic illustration of an optical setup is shown in S2 in ESI. Scattering images of individual Au NPs and stationary bubbles were obtained using a dark-field condenser (U-DCD (NA = 0.8 – 0.92), Olympus) and transmission imaging was performed with a bright-field condenser (IX-LWUCD, Olympus). Monochromatic CCD (Infinity 3-1 URM, Lumenera,) was used for both bright- and dark-field imaging. Transmission and scattering images of individual Au NPs are shown in Fig. S2 in ESI.

To characterize the optical properties of Au NPs, the forward light scattering spectra were measured by a fiber-coupled spectrometer (SD-2000, Ocean Optics). For all optical imaging, micro-spectroscopy, and laser illumination, a microscope objective (UPlanFl, 40× NA = 0.75, Olympus) was used. The excitation of a single Au NP was performed using a tightly-focused 532 nm CW DPSS laser (Exelsior 532, Spectra Physics). The spot size of the 532 nm laser light was estimated to be 0.9 μm in diameter (FWHM), by measuring the fluorescence intensity distribution of a thin amorphous film of fluorescent dyes on a well-cleaned coverslip under photoexcitation. To visualize the fluid convection by wide-field fluorescence imaging, a 488 nm CW laser (Exelsior 488, Spectra Physics) was employed as an excitation light source. The 488 nm CW laser was coaxially introduced into the optical path of the focused 532 nm CW laser. Irradiation of the two CW lasers was performed with mechanical shutters for each laser. For the wide-field fluorescence imaging, the laser power was set to 2.0 mW at the backport of the optical microscope. While monitoring the fluid convection by tracing the fluorescent polystyrene nanospheres (FL-beads), scattered laser light from the sample volume was blocked with a long-pass filter (BLP01-532R-25, Semrock). A time interval in fluorescence imaging was 36 ms: 6 ms for exposure time and 30 ms

for data acquisition. The laser power was measured using a photodiode power meter (S120UV & PM100, Thorlabs).

RESULTS and DISCUSSION

Formation of stationary bubbles under the CW laser heating.

First, we examined the stationary bubble formation induced by CW laser heating of a single Au NP with a diameter of 150 nm. Figure 1a shows the transmission image of a single Au NP without laser irradiation. The single Au NP with 150-nm-diameter was observed as a diffraction-limited point with a diameter of 0.6 μm at the center of the image corresponding to the irradiation spot. As shown in Figure 1b, c and d, under the CW laser irradiation at 532 nm, images larger than the diffraction limited size can be clearly observed with Airy diffraction patterns. Because the appearance of the Airy diffraction pattern is due to the disparity in refractive indices arising from the formation of a domain with a refractive index smaller than that of the surrounding water, these images show the generation of bubbles under this irradiation condition. These images were almost unchanged during the laser irradiation, indicating that the bubble is in a stationary state and the expansion was much faster than the time resolution in the present transmission and wide-field fluorescence imaging (typically a few tens of ms). From a heat conduction equation, temperature of a single NP can be estimated to reach a steady-state within a few μs under the CW laser illumination[40]. In addition, it was revealed, by means of time-resolved photothermal microscopy for a single Au NP, that the time scale on the expansion of vapor nanobubbles produced by CW laser heating was less than a few μs[41]. Accordingly, the expansion of the bubble was actually much faster than the time resolution in the present experimental condition. After stopping the irradiation, the bubble gradually decreased its size by transferring the gas molecules into the liquid phase[26]

and disappeared within several seconds. Interestingly, it has been reported that nanobubbles smaller than 200 nm in diameter produced by CW laser heating of a single Au NP repeat the periodic generation and contraction every ca. 500 ns; *i.e.* transient vapor bubbles can be produced even under CW laser illumination.[41] This behavior, however, is observed only in the limited experimental conditions. For the system with n-pentane ($T_{boiling}$: 309 K at atmospheric pressure) as a surrounding medium, this oscillating behavior was observed only in the case where the excitation intensity was just above the threshold of the bubble formation (*e.g.* 100 μW). Under the excitation condition with the intensity higher than the threshold, the stationary bubble was confirmed under CW laser illumination[41], as reported by many researchers[23,24,26]. The excitation condition in the present work is much higher than the threshold of the bubble formation and thus we can safely conclude that the microbubbles observed by diffraction-limited optical imaging, shown in Figure 1, are in a steady-state under CW laser illumination.

Figure 1e shows excitation intensity dependence of the bubble diameter that was defined as the circumference of the middle dark circle as shown in Figure 1c. The diameter, which were averaged values over 5-7 measurements, monotonically increases with an increase in the excitation power. Small deviations in the measurements at the same excitation power indicate good controllability of bubble diameter through CW laser heating of a single Au NP. Formation of bubbles was not observed at low excitation intensities < 10 mW μm^{-2} by optical transmission imaging. This might be due to the detection limit in the transmission image. For the evaluation of nanobubbles smaller than the diffraction limit, the dark-field imaging and light-scattering spectroscopy have been reported to be powerful tools[24]. Actually, we have conducted same experiment under dark-field illumination, and obtained results similar to those shown in Figure 1e (See Figure S3 in ESI). As will be discussed later, however, it is rather difficult to measure the

fluid convection around the stationary bubble with a diameter < 1 μm. Hence, we concentrate our discussion on the bubble observed at photoexcitation intensities ≥ 10 mW μm^{-2}.

Analysis of the condition for the stationary bubble formation.

The bubble in the stationary state is based on the balance between the energy input by a continuous photoabsorption of the Au NP and the release of heat from the inside to the outside of the bubble. Quantitative analyses of the stationary state could provide various physical parameters around the Au NP and the surrounding water. In actuality, these analyses were reported for micrometer-sized aggregates[23], thin films[31,32] and periodic arrays consisting of Au NPs[26]. Although these reports have yielded various parameters, rather complex structures of local heaters needed several assumptions on the surface temperature of the bubble[31], structure of the heat source and the boundary condition[26]. On the other hand, present system of a single isolated spherical Au NP could serve as one of ideal systems of the heat source, which could lead to better elucidation on the total amount of generated heat in the bubble and the temperature gradient at bubble surface.

Figure 2a shows the schematic representation of the calculation, which is based on the 1D heat conduction model consisting of a spherical NP immersed in a homogeneous medium. Under the actual experimental condition, however, surrounding environment of Au NPs consists of a glass substrate and water. To take into account the disparity in thermal conductivities between the two different media, we employed the effective thermal conductivity that has been devised for steady-state optical heating of a single Au NP supported on a dielectric substrate and immersed in medium[37,42]. Accordingly, the local temperature increase around a single Au NP is given by[10,37,40],

$$T(r) = \frac{C_{abs}\, I}{4\pi\, k_{eff}\, r} + T_{\infty} \quad (r = a) \qquad (1)$$

where C_{abs} [m^2] is the absorption cross section of an Au NP at excitation wavelength, I [W m^{-2}] peak power density, r [m] radial distance from NP center, a [m] nanoparticle radius, k_{eff} [W $m^{-1}K^{-1}$] effective thermal conductivity, and T_{∞} [K] ambient temperature. The peak power density I (mW μm^{-2}) is represented by $I = (P_{laser}\ (2.3546)^2) / 2\pi(\mathrm{fwhm})^2$, where P_{laser} [mW] is the laser power, and fwhm [μm] the laser beam diameter assuming a Gaussian beam profile. We used the effective thermal conductivity, k_{eff} of 0.8 [W $m^{-1}K^{-1}$], which value was reported[37,42] for the surrounding environment consisting of a glass substrate (k_{glass} = 1.0 [W $m^{-1}K^{-1}$]) and a water medium (k_{water} = 0.6 [W $m^{-1}K^{-1}$]). Effective refractive index (n_{eff}) of the surrounding medium was employed to calculate the C_{abs} from the Mie theory (See S.4 in ESI). Because of the temperature continuity at the interface between NP and medium under steady-state conditions, the temperature of NP (T_{NP}) can be obtained at the boundary where r equals to the radius of NP[43]. For pulsed laser hearing of Au NPs, it is known that there is a huge temperature gap at gold-water interface[44]. This discontinuity in temperature arises from the thermal boundary conductance at the surface. However, this parameter plays no role in steady-state regime[45]. Hence, the equation (1) is applicable to the calculation of the temperature of a single NP under the CW laser illumination. Temperature from the surface of NP to the surrounding medium was assumed to be inversely proportion with r as shown in Figure 2a, while it was assumed that the temperature in the NP was uniform due to the high thermal conductivity of gold (k_{gold} = 314 W $m^{-1}K^{-1}$). On the basis of this model with these parameters, we calculated the dependence of T_{NP} on peak power density.

Figure 2b shows the excitation intensity dependence of T_{NP} in the matrix consisting of

water/glass (blue solid line) and in the bubble/glass (red break line). In water/glass, T_{NP} linearly increased with an increase in peak power density, and reached the melting point of bulk gold ($T_{m.p.}$: 1337 K) at I = 28 mW μm^{-2}. As was shown in the previous section, the formation of the bubble was clearly confirmed at the peak power density ≥ 10 mW μm^{-2}. T_{NP} in the calculation at the peak power intensity of 10 mW μm^{-2} is 686 K, which is well above the spinodal temperature of water. Under CW illumination, it has been reported that the bubble formation takes place at the so called kinetic spinodal temperature, which is rather around 500 K.[22] The threshold temperature on the bubble formation in the present case seems to be overestimated compared with that of the literature[22], probably due to the resolution limit of optical imaging. In the experiment, the numerical aperture of the microscope objective employed is 0.75, which is not so high. It should be mentioned that the small nanobubbles invisible in transmission images were reported to appear at temperatures around 500 K[18,19]. Hence, as mentioned in the previous section, nanobubbles smaller than the diffraction-limited size might be produced at temperature range from 500 to 600 K (*i.e.*, I = 5 - 10 mW μm^{-2}). Accordingly, we conclude that our calculation on T_{NP} in water supports the mechanistic aspects on the bubble formation at temperatures around the kinetic spinodal temperature.[22]

After the bubble is generated, the Au NP is thermally insulated from water due to a poor thermal conductivity of the bubble, resulting in the huge T_{NP} jump[15]. Precise calculation of the T_{NP} jump in the bubble permits to estimate proper temperatures at the bubble surface, which is important for computational modeling of fluid convection. Effective thermal conductivity of 0.2 W m^{-1}K^{-1} was reported[37,39] for the steady-state optical heating of a single Au NP in the stationary bubble supported on the glass substrate. In addition, the absorption cross section of a single Au NP in a bubble, C_{abs}, is largely different owing to the change in the surrounding environment and

its temperature. Hence, we calculated T_{NP} in the stationary bubble, by taking into account the effective thermal conductivity of 0.2 W $m^{-1}K^{-1}$ and refractive index of 1.12 for the surrounding environment consisting of the bubble and the glass substrate (See details in S4 in ESI). The red dotted curve in Figure 2b shows that, at the threshold of bubble formation (10 mW μm^{-2}), T_{NP} jumps 686 to 2000 K. In the excitation intensity range from 10 to 60 mW μm^{-2}, maximum T_{NP} reached 7000 K which is much higher than the boiling point of gold ($T_{b.p.}$: 3129 K). At such high temperatures, thermal induced morphological changes of an Au NP are induced under laser illumination[15,46]. In our previous work, the dynamics on the CW-laser-induced morphological changes of a single Au NP was investigated by means of light scattering micro-spectroscopy and scanning electron microscopy[39]. The investigation revealed that the dynamics on morphological changes in the bubble can be divided into three steps (See details in S5 in ESI). i) At temperatures above $T_{b.p.}$, an original single Au NP was fragmented into a larger core NP and small satellite NPs owing to the evaporation from NP surface within a few milliseconds after bubble formation. ii) After a remarkable progression in evaporation of the core NP within a few seconds, the small fragments whose diameters ranging from 10 to 20 nm remained at the center of stationary bubble. iii) Owing to the much smaller C_{abs} of the fragments, a temperature of fragments (T_{FRG}) fell down below the $T_{m.p.}$. As a result, the fragments could work as stable heat sources to maintain the bubble in the steady state.

To estimate the increase in the local temperature for the step iii), collective photothermal effect of fragments in the bubble might be take into account. It has been reported that an infinite arrays of Au NPs exhibit collective photothermal effect in the entire region of the laser spot[43]. For the two-dimensionally dispersed Au NPs such as the fragments on a glass substrate, Baffou et al.

provided an analytical formula to evaluate the collective photothermal effect[47]. The formula ζ_2 is represented by $\zeta_2 = p^2 / 3LR$, where p [m] is the interparticle distance of the array, L [m] the characteristic length of the illuminated area, and R [m] radius of the nanoparticle. Smaller values of ζ_2 indicates significant contribution of the collective photothermal effect; for instance, the collective effect is negligible when $\zeta_2 > 1.0$, whereas $\zeta_2 < 0.1$ predicts the temperature distribution similar to that of laser heating of a metal thin film. From our previous investigation on the CW laser-induced fragmentation of a single Au NP in the bubble, we assumed R = 6 nm, p = 14 nm, and L = 400 nm (See S.5 in ESI). Applying these values to the equation, one can expect the moderate contribution of the collective effect. However, in principle, the collective effect appears only for the large number of NPs under illumination, such as the infinite periodic array[47]. In the present case, an averaged number of fragments in the bubble was only ca. 20 (See S.5 in ESI). Although the interparticle distance p is relatively small, we could estimate minor contribution of the collective photothermal effect owing to this small number. Thus, we neglected the collective effect and we employed the equation (1) for the temperature calculation of the fragments (T_{FRG}) in the bubble from.

To compute T_{FRG} from the equation (1), we assumed three typical diameters of the individual fragments (d = 6, 12, and 18 nm), because the nominal diameter of the fragments was obtained to be 12 $\pm$ 6 nm in our previous work (See S.5 in ESI)[39]. For individual fragments in the bubble, the absorption cross section, C_{abs}, was calculated on the basis of the Mie theory with the temperature-induced damping in LSPR (See details in S.6 in ESI). All parameters to compute T_{FRG} were thus obtained. Figure 2c shows the T_{FRG} as a function of the peak power density. T_{FRG} linearly increased with an increase in the peak power density. The temperature increase of a fragment with

an 18-nm diameter was several times larger than that for the fragment with a 6-nm diameter, reflecting the diameter dependent C_{abs}. Compared with T_{NP} for an Au NP with a 150-nm diameter as shown in Figure 2b, all T_{FRG} values were one order of magnitude lower because of the smaller C_{abs} of fragments. Hence, we conclude that the local temperature at the focal spot of the laser beam increases up to 500 K in the microbubble under intensive CW laser illumination. Thermally-induced fragmentation of Au NPs in the bubble has been already reported for the case of ultrashort pulsed laser[18,19,48] and CW laser[39] excitation. Temperature jump triggered by the bubble formation, however, has not been considered in previous reports on bubble-induced fluid convection. Thus, the local temperature increase in the stationary bubble under CW laser illumination was estimated on the basis of steady-state heat conduction equations.

Direct Detection of Fluid Convection around the bubble.

Using wide-field fluorescence microscopy of FL-beads, fluid convection around the bubble was directly detected. Figure 3 shows a series of snapshots on the formation of a bubble and subsequent fluid convection at the 532-nm excitation intensity of 40 mW μm^{-2} (see the movie in ESI). Before irradiation of the focused 532-nm CW laser, Brownian motion of FL-beads was observed as shown in Figure 3a. Once the bubble was produced by CW laser irradiation, individual FL-beads started to move toward the bubble (Fig. 3b and -c) and, a few second after the bubble formation, FL-beads exhibited a ring-like structure with a 3-μm diameter around the focal spot of 532 nm CW laser (Fig. 3d and -e). After forming the ring-like structure, the number of FL-beads gradually increased at the interface between water and the bubble, while keeping almost constant diameter of the ring-like structure (Fig. 3e to –h). These images clearly show spatial and temporal profiles of fluid convection around the bubble in such a manner that it whirls from the glass surface

to the upper part of the bubble as depicted in Scheme 1c.

So as to more quantitatively elucidate the convention, we have evaluated the convective velocity of FL-beads by tracking the location of individual fluorescence spots for each frame in the movie. As stated in the previous section, in the region within 20 μm in radial distance from the bubble center, the motion of FL-beads could not be detected at the excitation intensities larger than 40 mW μm^{-2} owing to much faster convective velocity than the time resolution of the fluorescence imaging. Accordingly, we measured the average velocity between the radial coordinates r=40 and r=20 μm. Figure 3i shows the dependence of the convective velocity on the peak power density. At peak power densities < 10 mW μm^{-2}, no clear convective motion of FL-beads was detected as already mentioned in previous sections. The velocity at the threshold peak power density (I = 10 mW μm^{-2}) of microbubble formation was 20 μm s^{-1} and it increases with increasing peak power density in the range of 10 to 30 mW μm^{-2}. In the range above 45 mW μm^{-2}, the convective velocity gradually saturated and reached 500 μm s^{-1}.

Figure 4a, -b, and –c show the optical images observed after the laser illumination at an excitation intensity of 40 mW μm^{-2} at 532 nm for 30 s. In all the optical images, a ring-like structure with the diameter similar to each other was observed at the position where the bubble existed. Since the ring-like structure could be clearly observed also in the fluorescence image, it is indicated that this ring-like structure consists of FL-beads. The excitation intensity dependence of the diameter of the ring-like structure is plotted in Fig. 4d, showing that the diameters increase with peak power density with no remarkable difference among the three methods of detection. Notably, the behavior on excitation intensity dependence of the ring-like structure is similar to that of the bubble diameter observed in transmission image shown in Fig. 1d. This similarity allows to

estimate a contact angle of the bubble on the glass substrate for the computational modeling of fluid convection (See S7. FEM geometry in ESI). In the previous reports, fabrication of a ring-like structure by bubble-induced convection has been already demonstrated[31–33]. Nevertheless, the formation of the ring-like structure was monitored only by static imaging methods with a lower time resolution. In the present work, fluid convection around the microbubble was clearly observed by wide-field fluorescence imaging of FL-beads with enough time resolution: especially from a viewpoint on the excitation intensity dependence of the convective velocity and the bubble diameter. On the other hand, it is worth mentioning that, within a small space, the driving force of the motion for small objects is not limited only to fluid convection. For instance, radiation pressure and thermophoresis are typical candidates. In the present irradiation condition of the CW laser, the radiation pressure is, however, negligible because the bubble formation was indispensable to induce the motion of FL-beads. Moreover, it has been reported that the thermophoretic force acting to nanoparticles in the temperature gradient is less than a few piconewton.[49] This value is much smaller than the drag force of fluid convection. Hence, we conclude that the motion of FL-beads around the bubble is driven by Marangoni convection.

Analysis of the fluid convection.

In this section, we show results of the fluid convection around the bubble on the basis of heat transfer and Navier-Stokes equations. As already mentioned in the introductory part, fluid convection is divided into natural convection and Marangoni one. Because the contribution from the natural convection has been reported[28,29] to be much smaller than that from the Marangoni one and, in actuality, the small contribution from the natural convection was quantitatively evaluated (See details, Figure 8), accordingly, we have assumed that the Marangoni convection entirely

dominates the fluid convection around the bubble. As already discussed in previous sections, tightly focused 532-nm CW laser induces an increase in local temperature around an Au NP and a bubble is produced in water (Scheme 1a and 1b). The temperature in the bubble is dependent on the distance from the Au NP. The highest temperature is attained at the focal spot of laser, while the surface temperature at the top of the bubble is the lowest due to the long distance from the heat source. The temperature difference in the bubble induces the gradient in the surface tension at the bubble surface and a large temperature coefficient of the surface tension gives rise to a strong shear force at the bubble surface[50]. This temperature dependent shear force at the bubble surface is an origin of Marangoni convection (Scheme 1c). Accordingly, temperature gradient at the bubble surface is essential for the analysis on the basis of heat transfer and Navier-Stokes equations.

Navier-Stokes equation is given by[51],

$$-\eta \nabla^2 \mathbf{u} + \rho \mathbf{u} \cdot \nabla \mathbf{u} + \nabla p = \mathbf{F} \qquad (2)$$

$$\nabla \cdot \mathbf{u} = 0 \qquad (3)$$

where η [kg m^{-1}s^{-1}], ρ [kg m^{-3}], $\mathbf{u}$ [m s^{-1}], and p [Pa] are respectively the dynamic viscosity, the density, the velocity vector, and the pressure. The **F** term represents external forces per unit volume. Temperature field for the equation 2 and 3 is given by[51] the following equation,

$$\nabla \cdot \left(-k \nabla T + \rho C_p T \, \mathbf{u}\right) = Q \quad (4)$$

Here, k [W m^{-1}K^{-1}], C_p [J kg^{-1} K^{-1}], and Q [W m^{-3}] are respectively the thermal conductivity, the

heat capacity, and the heat source term. As confirmed in the experiment results in previous sections, the bubble diameter and the convective velocity were in the stationary state under the laser illumination. In the actual calculation, we numerically solve these equations using the finite element method (FEM)[51]. A contact angle of the bubble on the glass substrate was determined from experimental results (S7 in ESI). At the maximum temperature (T_{FRG}) in the bubble shown in Fig. 2c, a large number of fragments were produced. For the treatment of the fragmented NPs, a point heat source was assumed for the source term Q in the equation 4 in this FEM analysis. Detailed geometry and boundary conditions for equations 2, 3, and 4 are given in S7 in ESI. Equations 2, 3, and 4 were numerically solved with COMSOL multiphysics (https://www.comsol.com/), which is a commercially available finite element method (FEM) solver.

Figure 5a shows 2D temperature distribution calculated for the peak power density at 46 mW μm^{-2} and the diameter of the bubble at 8.6 μm (corresponding to the results in Figures 1 and 2), indicating that the temperature is highest, 440 K, at the center of the bubble and lower temperature is observed at the surface area. Moreover, the surface temperature at the top of the bubble is slightly lower than the interfacial region between water and the glass substrate. To more precisely clarify the temperature gradients, we plotted temperature profiles along x-coordinate at various heights (y-distance) from the glass surface (Fig. 5b). Whereas a steeper temperature gradient is observed within the initial 10 nm, the temperature in the bubble decreases with an increase in the y-distance to 500 nm. At the surface, temperature was ca. 300 K. Outside the bubble, temperature gradually decreased with x-distance at each y-distance, and reached the room temperature (293 K) at an x-distance of 100 μm. Significant reductions in the temperature gradient outside the bubble is ascribable to the higher thermal conductivity of water (0.6 W $m^{-1}K^{-1}$)

compared with that of air (0.024 W $m^{-1}K^{-1}$). Govorov *et al.* have provided analytical solutions to calculate the 1D steady-state heat conduction for a system consisting of a single NP, polymer shell layer, and a surrounding liquid medium[43]. In this case, the temperature gradient in a polymer matrix was proved to be steeper than that in a medium owing to a poor thermal conductivity of the polymer. Thus we have concluded that the computational results of 2D temperature distribution are consistent with the heat conduction theory. At the same time, the 2D distribution of convective velocity was obtained on the basis of temperature calculation.

Figure 5c shows the calculated 2D distribution of the convective velocity. Red arrows in the figure indicate normalized velocity vectors. The whirling motion of convection flow around the bubble was clearly shown by the velocity vectors; this result well reproduces the experimental one on the convective motion of FL-beads observed by wide-field fluorescence imaging (Fig. 3). Figure 5d shows the velocity profiles along *x*-axis at various *y*-distances, indicating that the convective velocity monotonically increased with y-distance. While the convective velocity larger than 1.0×10^4 μm s^{-1} was observed at the position adjacent to the bubble surface owing to the huge temperature gradient (Fig. 5c), it decreased to 10 μm s^{-1} with increasing *x*-distance up to several tens of micrometers. This drastic reduction in the velocity at a longer *x*-distance well agrees with the experimental result that the convective motion of FL-beads was only detectable within 40 μm from the bubble center in radial distance. As shown above, numerical simulation revealed the strong x-distance dependence of the convective velocity with 4 orders of magnitude. From Figure 5c, we can safely conclude that the permanent sticking of FL-beads observed in Figure 4 is due to strictly localized velocity maximum being in contact with the bubble, which markedly differs from the situation of natural fluid convection (see Figure 8).

In order to comprehensively elucidate the driving force of Marangoni convection, we investigated the excitation intensity dependence of the convective velocity for the bubble with 8.6-μm diameter. Figure 6a shows the temperature calculated at three points; the point heat source, the top of the bubble, and the bottom under various peak power densities. The temperature at the heat source linearly increased up to 500 K with an increase in the peak power density. In contrast, the temperature at the top and bottom of the bubble increases only less than 10 K from the room temperature (293 K). As already discussed in the previous section, these temperature differences arose from the disparity in thermal conductivities of the materials.

Because the increase in the temperature at the top and the bottom of the bubble is small, the difference in the temperature between the top and bottom of the bubble (ΔT_{BT}) is not large. The maximum ΔT_{BT} was only 4 K even at a peak power density of 60 mW μm^{-2} in this calculation. As stated in previous sections, Marangoni convection is quite sensitive to ΔT_{BT} because the shear force is strongly dependent on the temperature gradient at the bubble surface. To quantitatively elucidate the effect of ΔT_{BT}, excitation intensity dependence of convective velocity was examined. Figure 6c shows the convective velocities at a constant *y*-distance of 500 nm and various *x*-distances as a function of ΔT_{BT}. In this plot, ΔT_{BT} was obtained from the calculated result shown in Figure 6b. At all *x*-distances, the convective velocity increases to 1.0×10^2 μm s^{-1} as ΔT_{BT} increases to 4 K. In this calculation, ΔT_{BT} of 3.4 K (= 46 mW μm^{-2}) resulted in the convective velocities of 40, 90, 280 μm s^{-1} for the *x*-distance of 40, 30, 20 μm, correspondingly. In the experiment, a similar convective velocity of 250 ± 67 μm s^{-1} was obtained at the same peak power density of 46 mW μm^{-2}. The agreement in the convective velocities between the experimental and calculated results supports that the fluid convection around the bubble is mainly regulated by the ΔT_{BT} less than several Kelvin

at the bubble surface. (See convective velocities at other heights, S8 in ESI)

To more clearly confirm the role of ΔT_{BT}, we investigated the relation between the convective velocity and the size of the bubble. Diameters and contact angles of the bubble for the numerical simulation were determined by referring the experimental results in the present work. Temperature at the point heat source as a function of peak power density was estimated from Fig. 2c for each bubble diameter. As performed in previous sections, 2D numerical simulation on heat transfer and fluid convection was carried out. Figure 7a shows the convective velocities at a constant *y*-distance of 500 nm and three *x*-distances as a function of the bubble diameter (See convective velocities at other y-distances, S.9 in ESI). Experimental results are also plotted for the comparison. Convective velocities at each *x*-distance noticeably increased as the bubble expanded to 10 μm in diameter. Further expansion in the bubble diameter resulted in a gradual saturation of the convective velocity around 1.0×10^3 μm s^{-1}. Experimental plots are reproduced by the calculated convective velocity at a *x*-distance of 20 μm. In particular, the characteristic rise of experimental results is well reproduced by the calculated curve in the diameter range from 2 to 10 μm.

To elucidate an origin of the gradual saturation in convective velocity, ΔT_{BT} between the top and bottom of the bubble was extracted from Fig. 7a. Figure 7b shows ΔT_{BT} as a function of the bubble diameter. ΔT_{BT} increased 2.4 K to 2.8 K as the bubble expanded to 10 μm in diameter. In contrast, an increase in ΔT_{BT} was not remarkable at the bubble diameters larger than 10 μm, indicating that the gradual saturation in convective velocity is due to the bubble diameter dependence of ΔT_{BT}. This result confirms again that the Marangoni convection is sensitive to the small difference of ΔT_{BT}.

Finally, we show computational results of the natural convection to make a quantitative comparison with Marangoni convection. To calculate the natural convection, the same geometry shown in S7 in ESI was used. However, the shear force applied at the bubble surface was canceled to clarify the contribution of natural convection. Instead, a volume force to describe the buoyancy force in water domain is given by[29]

$$F = \begin{pmatrix} F_x \\ F_y \end{pmatrix} = \begin{Bmatrix} 0 \\ \alpha g \rho (T - T_{ref}) \end{Bmatrix} \qquad (5)$$

where α [K^{-1}] is the thermal expansion coefficient of water, g [m s^{-2}] gravitational acceleration, ρ [kg m^{-3}] density of water, and T_{ref} [K] the reference temperature (room temperature, in this case). The temperature dependence of α was not considered. In the following calculation, the bubble diameter was fixed at 8.6 μm, and the computational variable was only the surface temperature of the bubble. Figure 8a and -b show 2D temperature distribution and corresponding velocity field at a fixed bubble temperature of 373 K. The 2D temperature distribution in Figure 8a shows the concentric temperature gradients from the bubble center. The corresponding convective flow whirls in water domain as shown in Figure 8b, which is typical flow of the natural convection[29]. The highest convective velocity, 40 μm s^{-1}, was obtained at a x-distance of 0 μm and a y-distance of 120 μm (around the center of the water domain). In addition, the convective velocities at the side of the bubble (around x = ± 100 μm and y = 50 μm) were faster than that at other region. Figure 8c shows the convective velocities at the center and the side as a function of the bubble temperature (T_{Bubble}). Almost linear behavior in the convective velocity can be ascribed to the constant thermal expansion coefficient of water. Although the utmost bubble temperature of

373 K (the bulk boiling temperature of water) was applied, the convective velocity adjacent to the glass surface was less than 1 to 2 μm s^{-1}. Therefore, we have concluded that the contribution of natural convection is negligible because of the lower surface temperature in reality.

CONCLUSION

In the present study, we have elucidated the following properties of the stationary microbubble and subsequent Marangoni convection under CW laser illumination.

i) The diameter of bubble increased with peak power density.

ii) No detectable convection was observed without the formation of microbubble.

iii) Convective velocity increased to 1.0×10^3 μm s^{-1} with ΔT_{BT} at the bubble surface. Effective convection took place within 100 μm from the bubble center in radial distance.

iv) Once the bubble diameter exceeded a certain size, convective velocity gradually saturated owing to the gradual saturation in ΔT_{BT} at the bubble surface.

v) Owing to lower temperatures at the bubble surface, the contribution of natural convection was minor.

Basically, above findings are also applicable when an aggregates or a thin film consisting of Au NPs is employed as a heat source. The surface temperature of the bubble was estimated to be around 300 K, which is much lower than the bulk boiling point of water. This can be advantageous to assemble or manipulate soft materials which cannot withstand at high temperatures.

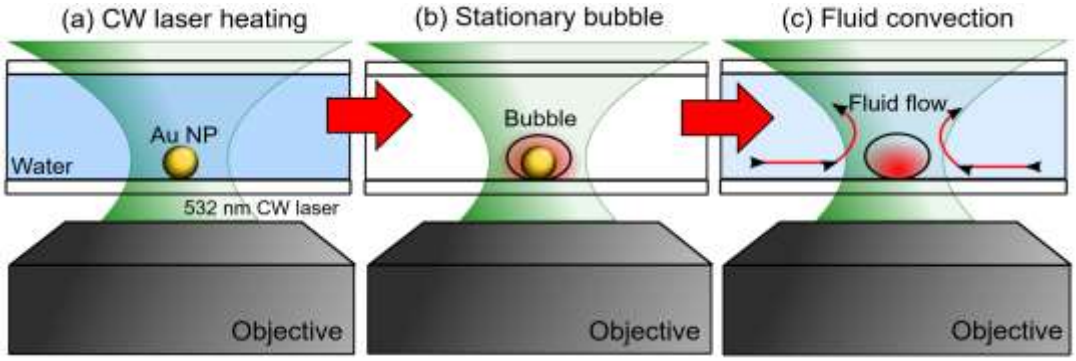

Scheme 1. Schematic illustrations of time evolution of an Au NP supported on a substrate under CW laser illumination.

Figure 1

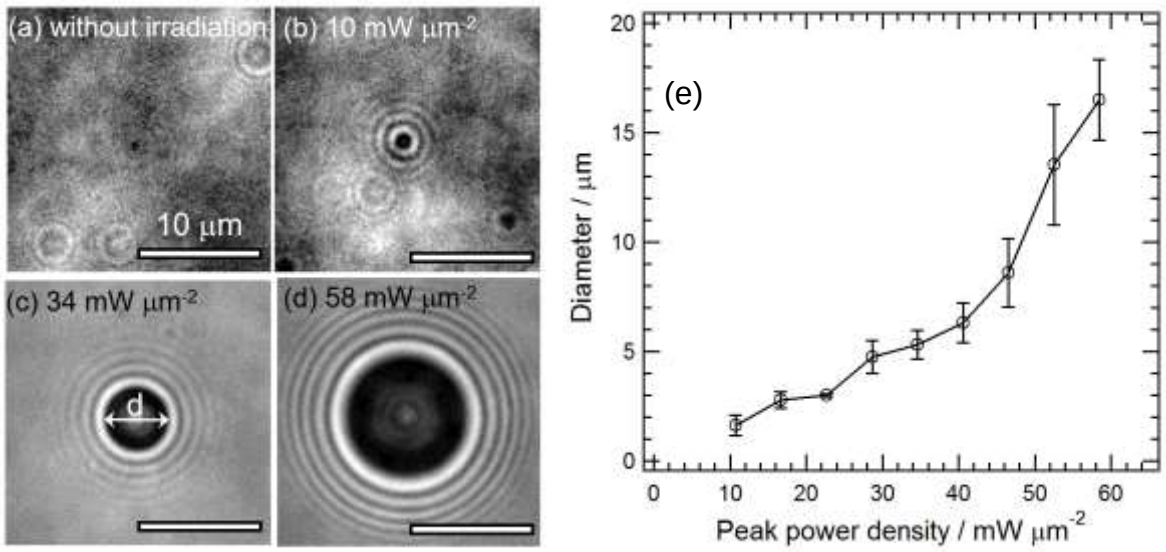

Figure 1. (a-d) Optical transmission images of the bubble formation at the laser powers of 0, 10, 34, and 58 mW μm^{-2}. (e) The bubble diameter as a function of laser peak power density.

Figure 2

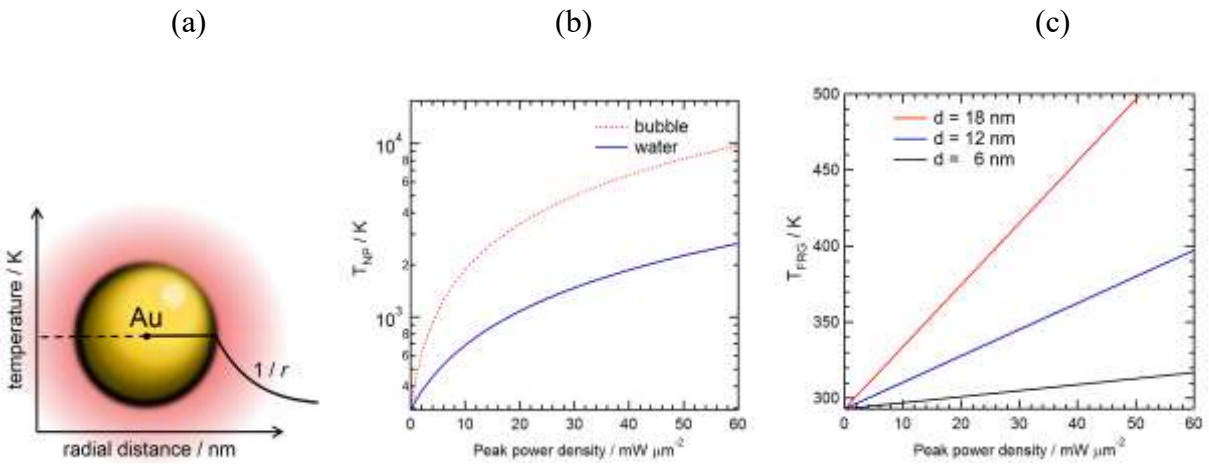

Figure 2. (a) Schematic representation of steady-state heating of a single Au NP immersed in a homogeneous medium. (b) Relation between the peak power density and T_{NP} calculated by the equation 1 for a 150-nm-diameter Au NP in the bubble and water. (c) Relation between the peak power density and T_{FRG} calculated by the equation 1 for fragments of Au NP in the bubble.

Figure 3

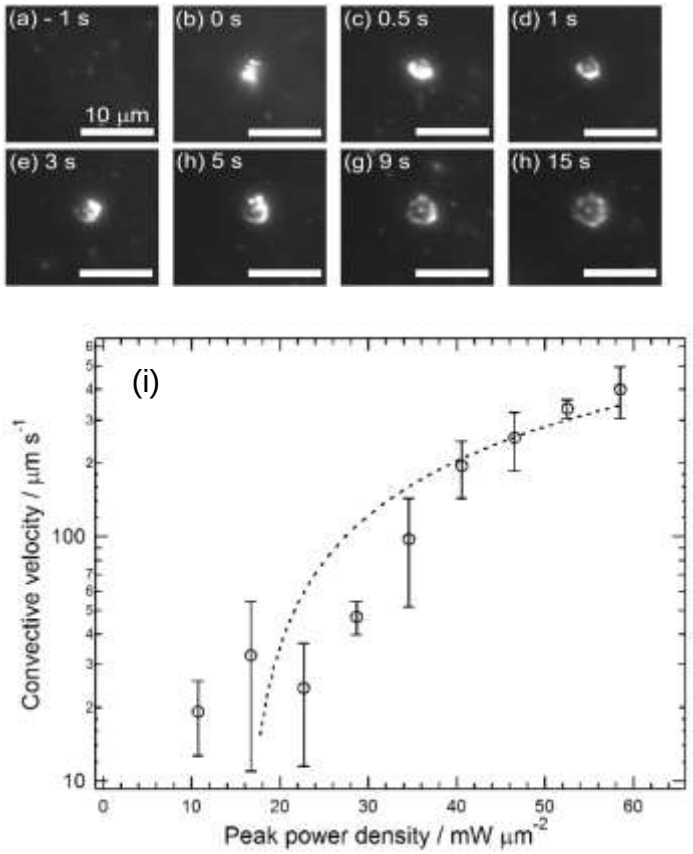

Figure 3. (a-h) A time course of fluorescence images of FL-beads around the stationary bubble at the laser peak power density I = 40 mW μm^{-2}. (i) The convective velocity as a function of laser peak power density determined with wide-field fluorescence imaging of FL-beads. The dotted black line is included as a visual guide.

Figure 4

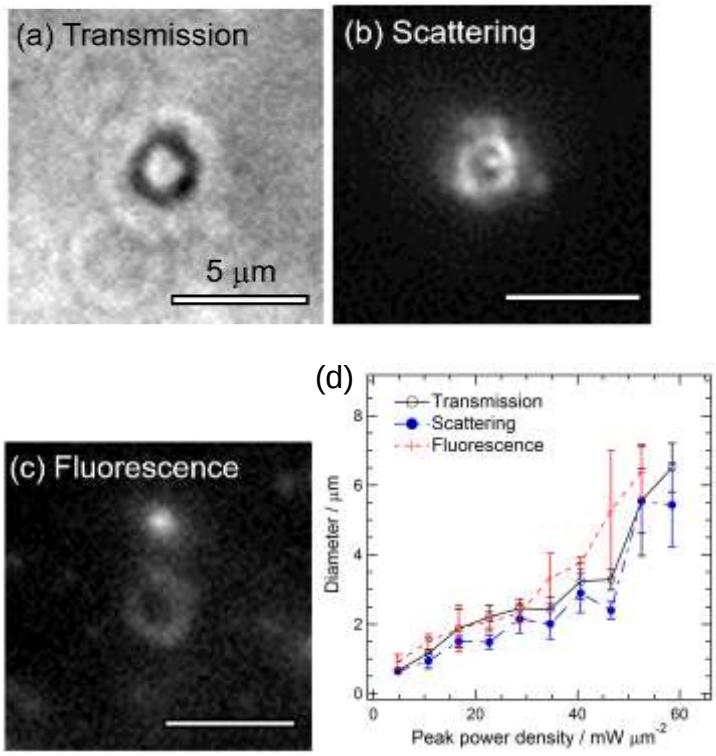

Figure 4. Optical microscope images of a ring-like structure monitored after laser irradiation at I = 40 mW μm^{-2}: (a) transmission, (b) scattering, and (c) fluorescence. (d) Relationship between laser peak power density and the diameter of a ring-like structure obtained with transmission, scattering, and fluorescence imaging.

Figure 5

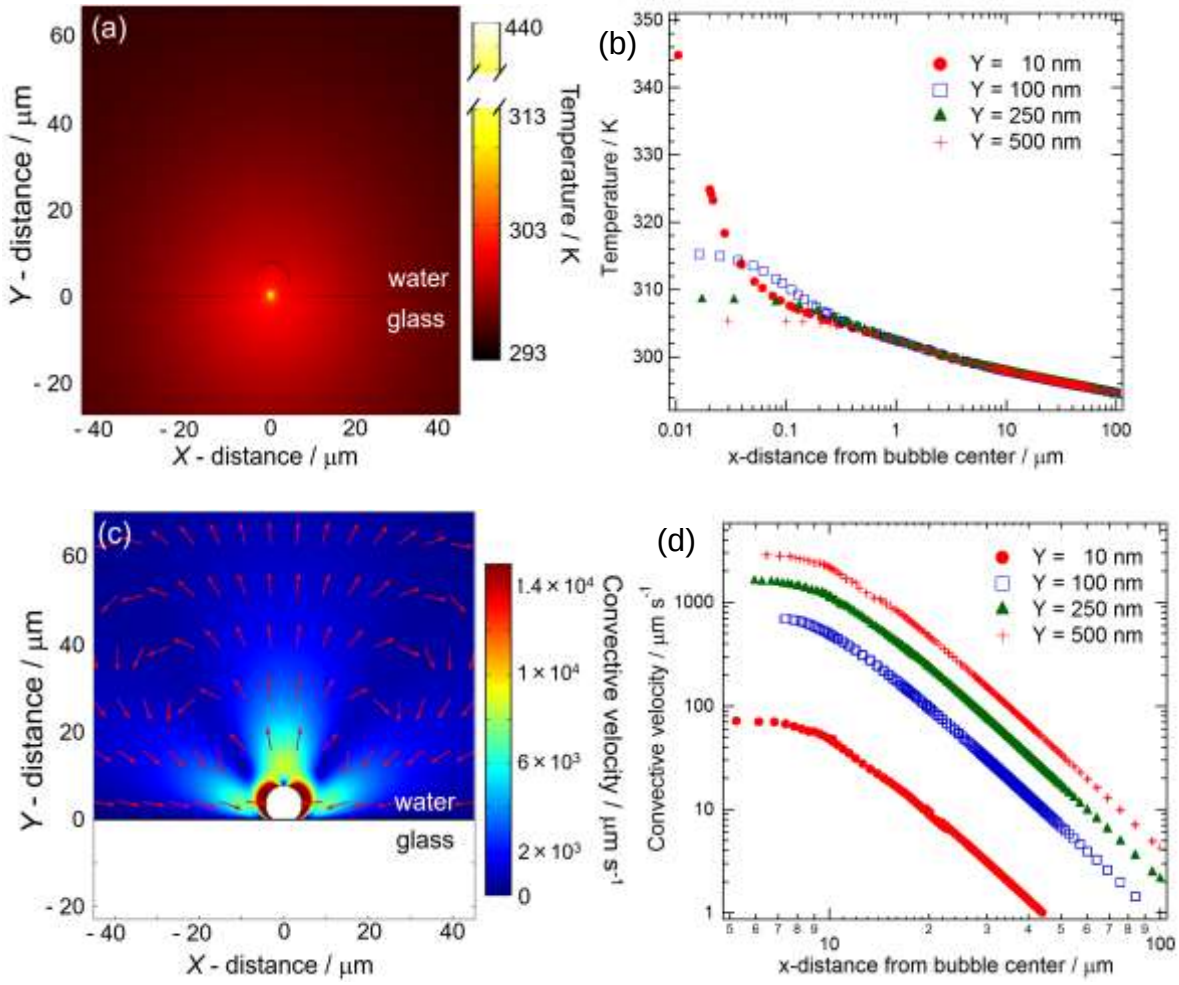

Figure 5. Computational 2D temperature distribution (a) and velocity field (b) for the system consisting of the 8.6-μm-diameter bubble, water, and the glass substrate: The peak power density of 46 mW μm^{-2} was applied. (c) Temperature profiles along *x*-axis at various *y*-distances obtained from 2D temperature distribution. (d) Velocity profiles along *x*-axis at various *y*-distances obtained from 2D velocity field.

Figure 6

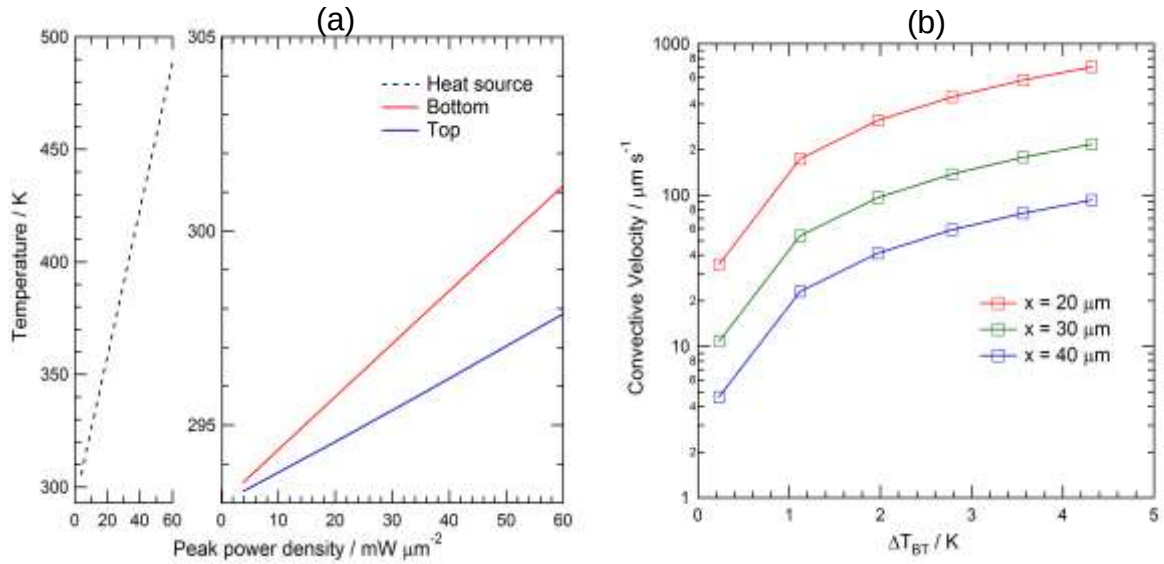

Figure 6. (a) Calculated temperatures at the heat source, the bottom of the bubble, and the top of the bubble as a function of laser peak power density for the 8.6-μm-diameter bubble. (b) Convective velocities *vs* ΔT_{BT}, calculated at a constant *y*-distance of 500 nm for three different *x*-distances.

Figure 7

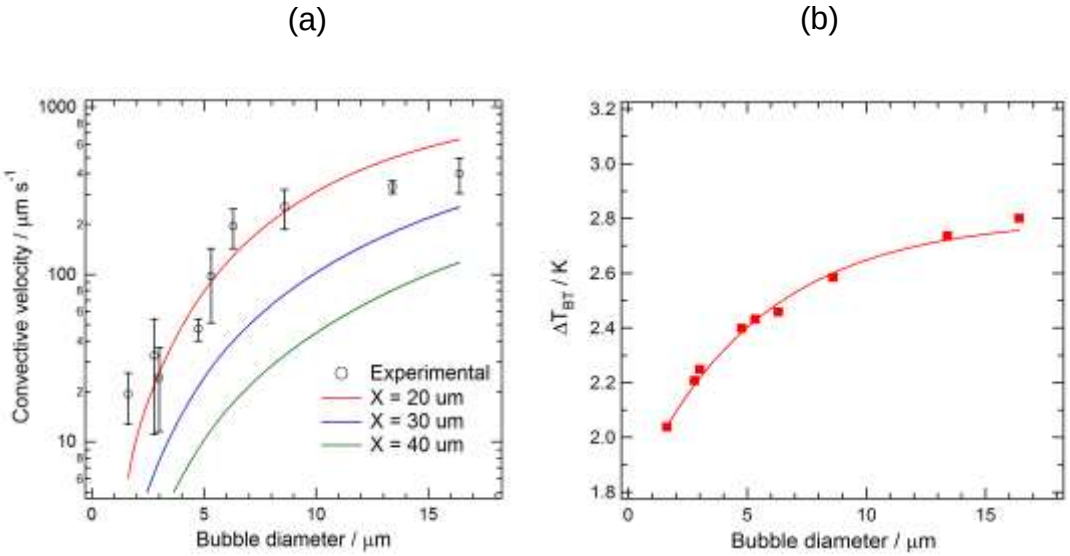

Figure 7. (a) The convective velocity as a function of the bubble diameter at *y*-distances of 500 nm, calculated for three different *x*-distances. Experimental data is also plotted together. (b) ΔT_{BT} at the bubble surface as a function of the bubble diameter calculated from Fig. 7a.

Figure 8

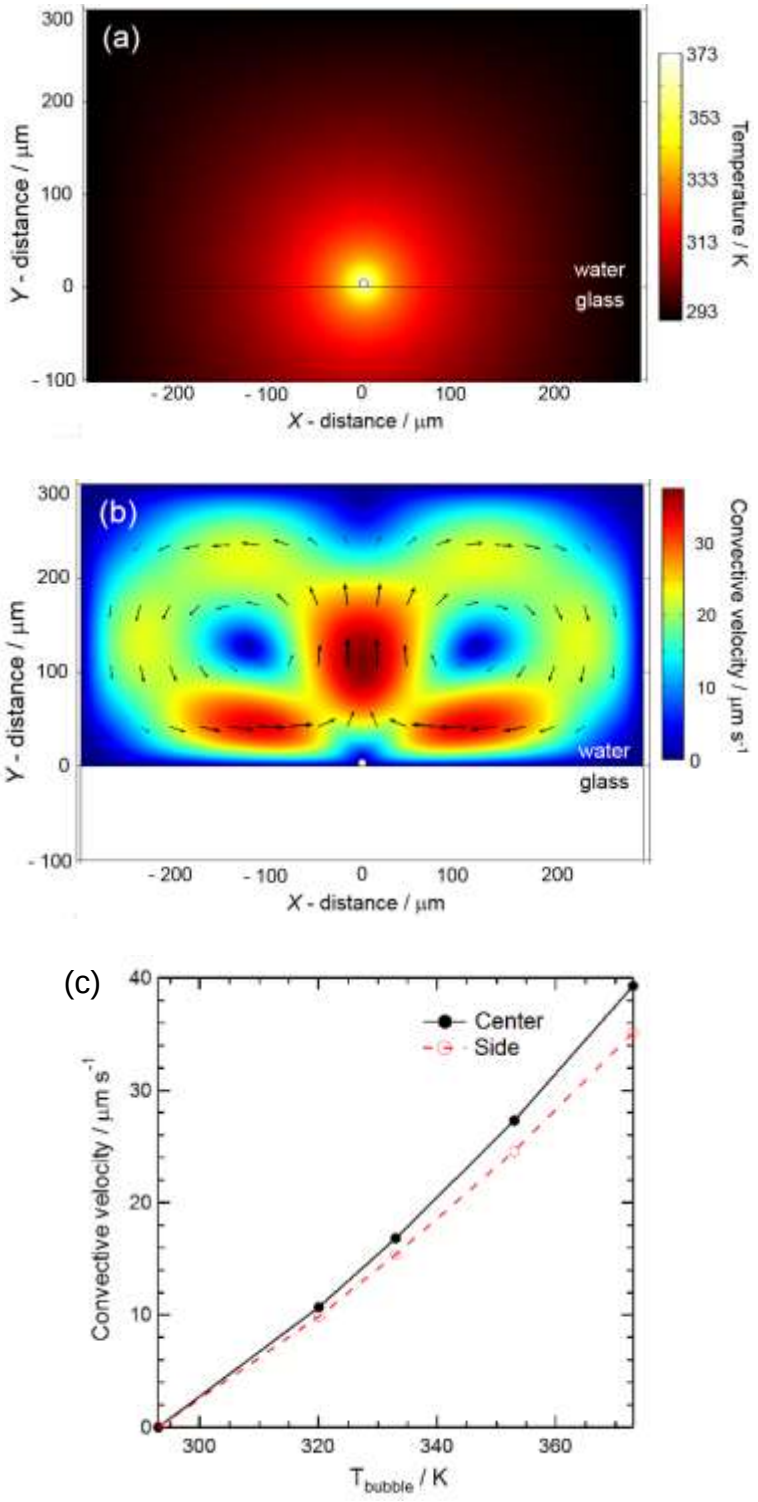

Figure 8. (a) Computational 2D temperature distribution and (b) velocity field for the system

consisting of the 8.6-μm-diameter bubble, water, and the glass substrate. The surface temperature of the bubble was set to 373 K. (c) Calculated convective velocity at the center of water domain and the side of the bubble as a function of the surface temperature of the bubble (T_{bubble}).

ACKNOWLEDGMENTS

This study was financially supported by JSPS KAKENHI Grant Number JP26107002, JP15K13625, 16H03827, JP26288009, and JP16H06505. K.S. was supported by Grant-in-Aid for JSPS Fellows Grant Number JP16J01715

REFERENCES

1 S. Link and M. A. El-Sayed, *Annu. Rev. Phys. Chem.*, 2003, **54**, 331–366.

2 P. Mulvaney, *Langmuir*, 1996, **12**, 788–800.

3 N. J. Halas, S. Lal, W.-S. Chang, S. Link and P. Nordlander, *Chem. Rev.*, 2011, **111**, 3913–3961.

4 K. Watanabe, D. Menzel, N. Nilius and H. J. Freund, *Chem. Rev.*, 2006, **106**, 4301–4320.

5 K. Ueno and H. Misawa, *J. Photochem. Photobiol. C*, 2013, **15**, 31–52.

6 X.-M. Qian and S. M. Nie, *Chem. Soc. Rev.*, 2008, **37**, 912–920.

7 P. L. Stiles, J. A. Dieringer, N. C. Shah and R. P. Van Duyne, *Annu. Rev. Anal. Chem.*, 2008, **1**, 601–626.

8 H. Inouye, K. Tanaka, I. Tanahashi and K. Hirao, *Phys. Rev. B*, 1998, **57**, 11334.

9 G. V Hartland, *Chem. Rev.*, 2011, **111**, 3858–3887.

10 A. O. Govorov and H. H. Richardson, *Nano Today*, 2007, **2**, 30–38.

11 N. S. Abadeer and C. J. Murphy, *J. Phys. Chem. C*, 2016, **120**, 4691-4716.

12 D. Boyer, P. Tamarat, A. Maali, B. Lounis and M. Orrit, *Science*, 2002, **297**, 1160–1163.

13 M. Selmke, M. Braun and F. Cichos, *ACS Nano*, 2012, **6**, 2741–2749.

14 A. S. Urban, S. Carretero-Palacios, A. A. Lutich, T. Lohmüller, J. Feldmann and F. Jäckel, *Nanoscale*, 2014, **6**, 4458–4474.

15 S. Hashimoto, D. Werner and T. Uwada, *J. Photochem. Photobiol. C*, 2012, **13**, 28–54.

16 E. Y. Lukianova-Hleb, X. Ren, R. R. Sawant, X. Wu, V. P. Torchilin and D. O. Lapotko, *Nat. Med.*, 2014, **20**, 778–84.

17 E. Y. Lukianova-Hleb, Y.-S. Kim, I. Belatsarkouski, A. M. Gillenwater, B. E. O'Neill and D. O. Lapotko, *Nat Nanotechnol.*, 2016, **11**, 525-532.

18 A. Siems, S. A. L. Weber, J. Boneberg and A. Plech, *New J. Phys.*, 2011, **13**, 043018.

19 T. Katayama, K. Setoura, D. Werner, H. Miyasaka and S. Hashimoto, *Langmuir*, 2014, **30**, 9504–9513.

20 E. Lukianova-Hleb, Y. Hu, L. Latterini, L. Tarpani, S. Lee, R. a. Drezek, J. H. Hafner and D. O. Lapotko, *ACS Nano*, 2010, **4**, 2109–2123.

21 K. Sasikumar and P. Keblinski, *J. Chem. Phys.*, 2014, **141**, 234508.

22 K. Metwally, S. Mensah and G. Baffou, *J. Phys. Chem. C*, 2015, **119**, 28586-28596.

23 D. Hühn, A. Govorov, P. R. Gil and W. J. Parak, *Adv. Funct. Mater.*, 2012, **22**, 294–303.

24 Z. Fang, Y.-R. Zhen, O. Neumann, A. Polman, F. J. García de Abajo, P. Nordlander and N. J. Halas, *Nano Lett.*, 2013, **13**, 1736-1742.

25 M. T. Carlson, A. J. Green and H. H. Richardson, *Nano Lett.*, 2012, **12**, 1534–1537.

26 G. Baffou, J. Polleux, H. Rigneault and S. Monneret, *J. Phys. Chem. C*, 2014, **118**, 4890–4898.

27 M. Wang, C. Zhao, X. Miao, Y. Zhao, J. Rufo, Y. J. Liu, T. J. Huang and Y. Zheng, *Small*, 2015, **11**, 4423–4444.

28 J. S. Donner, G. Baffou, D. McCloskey and R. Quidant, *ACS Nano*, 2011, **5**, 5457–5462.

29 B. J. Roxworthy, A. M. Bhuiya, S. P. Vanka and K. C. Toussaint, *Nat. Commun.*, 2014, **5**, 3173.

30 G. L. Liu, J. Kim, Y. Lu and L. P. Lee, *Nat. Mater.*, 2006, **5**, 27–32.

31 L. Lin, X. Peng, Z. Mao, W. Li, M. N. Yogeesh, B. B. Rajeeva, E. P. Perillo, A. K. Dunn, D. Akinwande and Y. Zheng, *Nano Lett.*, 2015, **16**, 701–708.

32 S. Fujii, K. Kanaizuka, S. Toyabe, K. Kobayashi, E. Muneyuki and M. A. Haga, *Langmuir*, 2011, **27**, 8605–8610.

33 V. I. Yusupov, S. I. Tsypina and V. N. Bagratashvili, *Laser Phys. Lett.*, 2014, **11**, 116001.

34 Y. Nishimura, K. Nishida, Y. Yamamoto, S. Ito, S. Tokonami and T. Iida, *J. Phys. Chem. C*, 2014, **118**, 18799–18804.

35 K. Namura, K. Nakajima, K. Kimura and M. Suzuki, *Appl. Phys. Lett.*, 2015, **106**, 43101.

36 T. Uwada, S. Fujii, T. Sugiyama, A. Usman, A. Miura, H. Masuhara, K. Kanaizuka and M. Haga, *ACS Appl. Mater. Interfaces*, 2012, **4**, 1158–1163.

37 K. Setoura, Y. Okada, D. Werner and S. Hashimoto, *ACS Nano*, 2013, **7**, 7874–7885.

38 H. Yamauchi, S. Ito, K. Yoshida, T. Itoh, Y. Tsuboi, N. Kitamura and H. Miyasaka, *J. Phys. Chem. C*, 2013, **117**, 8388–8396.

39 K. Setoura, Y. Okada and S. Hashimoto, *Phys. Chem. Chem. Phys.*, 2014, **16**, 26938–26945.

40 P. Keblinski, D. G. Cahill, A. Bodapati, C. R. Sullivan and T. A. Taton, *J. Appl. Phys.*, 2006, **100**, 54305.

41 L. Hou, M. Yorulmaz, N. R. Verhart and M. Orrit, *New J. Phys.*, 2015, **17**, 13050.

42 G. Baffou, R. Quidant and C. Girard, *Phys. Rev. B*, 2010, **82**, 165424.

43 A. O. Govorov, W. Zhang, T. Skeini, H. Richardson, J. Lee and N. A. Kotov, *Nanoscale Res. Lett.*, 2006, **1**, 84–90.

44 Z. Ge, D. G. Cahill and P. V. Braun, *J. Phys. Chem. B*, 2004, **108**, 18870–18875.

45 G. Baffou and H. Rigneault, *Phys. Rev. B*, 2011, **84**, 035415.

46 G. González-Rubio, A. Guerrero-Martínez and L. M. Liz-Marzán, *Acc. Chem. Res.*, 2016, **49**, 678-686.

47 G. Baffou, P. Berto, E. Bermúdez Ureña, R. Quidant, S. Monneret, J. Polleux and H. Rigneault, *ACS Nano*, 2013, **7**, 6478–6488.

48 D. Werner, T. Ueki and S. Hashimoto, *J. Phys. Chem. C*, 2012, **116**, 5482–5491.

49 J. Gargiulo, S. Cerrota, E. Cortés, I. L. Violi and F. D. Stefani, *Nano Lett.*, 2016, **16**, 1224–1229.

50 N. b. Vargaftik, B. N. Volkov and L. D. Voljak, *J. Phys. Chem. Ref. Data*, 1983, 12, 817–820.

51 F. Mechighel, M. El Ganaoui, B. Pateyron and M. Kadja, *Proceedings COMSOL Conference*, 2007, Grenoble, France, 24-25.